Computers, Materials & Continua

Tech Science Press

https://doi.org/10.32604/cmc.2026.086403

ARTICLE

Structure-Informed Machine Learning for Multi-Property Prediction of NBT-Based Lead-Free Piezoceramics

Yalong Liang[1], **Xiaohui Yuan**[1], **Yuning Han**[2] **and Pei Li**[3,*]

[1]School of Architecture and Civil Engineering, Xinyang Normal University, Xinyang, China
[2]School of Materials Science and Engineering, Henan University of Science and Technology, Luoyang, China
[3]Centre for Industrial Mechanics, Institute of Mechanical and Electrical Engineering, University of Southern Denmark, Sønderborg, Denmark

*Corresponding Author: Pei Li. Email: lipei@sdu.dk

Received: 29 May 2026; Accepted: 05 August 2026; Published: 15 September 2026

ABSTRACT: NBT-based lead-free piezoceramics are promising alternatives to Pb-containing materials, yet their functional properties arise from complex and coupled composition–processing–structure–property relationships. Here, we develop a structure-informed machine learning framework to predict and interpret the piezoelectric coefficient d_{33}, depolarization temperature T_d, and relative dielectric permittivity ε_r. A database of 214 records from 34 publications was compiled, including 204 records for model development and 10 records for independent literature validation. The correlation analysis involved 38 variables, including 35 candidate input descriptors and three target properties. After Pearson correlation-based redundancy filtering, 30 nonredundant input descriptors were retained for model development. To incorporate physically meaningful structural information, structural feature variables were introduced to describe phase-boundary characteristics, local lattice distortion, and effective phase state, thereby improving the interpretability of composition/processing–property relationships. ExtraTreesRegressor (ETR), deep neural networks (DNNs), and residual network (ResNet)-style multilayer perceptrons (MLPs) were evaluated using random five-fold cross-validation, while Bayesian neural networks (BNNs) were used for uncertainty quantification and SHAP analysis was used to identify influential descriptors. Under random five-fold cross-validation, the best-performing models achieved R^2 values of 0.79, 0.89, and 0.90 for d_{33}, T_d, and ε_r, respectively, suggesting that structural descriptors provide informative physical features for property prediction. SHAP results further highlighted the important role of processing-related descriptors, particularly calcination parameters, in tuning dielectric responses. This framework provides a physically interpretable and uncertainty-aware strategy for candidate screening and optimization of high-performance NBT-based lead-free piezoceramics.

KEYWORDS: Lead-free piezoelectric ceramics; NBT-based ceramics; structure-informed machine learning; composition–processing–structure–property relationship; morphotropic phase boundary; interpretable materials informatics

1 Introduction

Piezoelectric ceramics enable efficient electromechanical energy conversion and have been widely used in sensors, actuators, transducers, microelectronic devices, and related applications. In recent years, machine-learning-based methods have been increasingly applied to the property prediction and uncertainty quantification of lead-free piezoelectric ceramics [1–3]. Conventional lead-based piezoelectric ceramics represented by $Pb(Zr,Ti)O_3$ (PZT) have long dominated this field owing to their outstanding piezoelectric

response and thermal stability. However, the environmental pollution and potential health hazards associated with lead oxide volatilization during processing and long-term service severely limit their sustainable development. Therefore, the development of high-performance lead-free piezoelectric ceramics has become an important research direction [4–6].

Among the various lead-free piezoelectric candidates, $Bi_{0.5}Na_{0.5}TiO_3$(NBT)-based ceramics, namely NBT-based ceramics, have attracted considerable attention owing to their strong ferroelectricity, relatively high Curie temperature, and tunable phase structures [7,8]. By forming solid solutions with end members such as $BaTiO_3$ and $SrTiO_3$, NBT-based ceramics can exhibit diverse structural states, including rhombohedral-like, tetragonal-like, pseudocubic, nonergodic relaxor (NER), and mixed phase-boundary states. Such phase-structure evolution has a pronounced influence on their piezoelectric, dielectric, and electric-field-induced strain responses [8,9]. In particular, near morphotropic phase boundaries (MPBs) or relaxor phase boundaries, enhanced structural instability facilitates polarization rotation, domain-wall motion, and electric-field-induced phase transitions, thereby improving the electromechanical response [10,11]. However, the macroscopic properties of NBT-based ceramics are not governed by a single factor, but are strongly coupled with composition, ionic-radius mismatch, A-/B-site disorder, processing conditions, phase-structure state, microstructural characteristics, and poling conditions. Therefore, conventional trial-and-error optimization is inefficient in revealing such complex nonlinear composition–processing–structure–property relationships [12].

In recent years, the integration of machine learning (ML) and materials informatics has provided a new paradigm for property prediction, candidate screening, and structure–property relationship analysis in complex functional materials [13,14]. Compared with conventional empirical models, ML can help extract nonlinear correlations among composition, processing, structure, and properties from experimental data, and has shown potential in crystal-structure prediction, perovskite stability assessment, ferroelectric materials design, and piezoelectric property prediction [15–17]. For NBT-based ceramics, compositional information alone is insufficient to fully describe the origin of their functional properties. Incorporating physically relevant descriptors, such as ionic-radius statistics, tolerance factor, configurational entropy, processing parameters, phase-structure labels, and poling conditions, is expected to provide a more comprehensive representation of the coupled composition–processing–structure–property relationships in these systems [18–21].

In our recent study [1–3], a physics-informed and uncertainty-aware machine-learning framework was developed for KNN- and NBT-based lead-free piezoceramics, integrating deterministic neural-network models [22–25], Bayesian uncertainty quantification, and Shapley additive explanations (SHAP)-based interpretation for interpretable d_{33} prediction [26–29]. Building on this methodological foundation, the present work further incorporates ExtraTreesRegressor (ETR) as a robust ensemble baseline, which can improve prediction stability by randomizing both feature selection and split thresholds and is therefore well suited for heterogeneous literature-derived materials datasets [30].

More importantly, this study extends the previous framework to NBT-based lead-free piezoceramics by developing a structure-informed machine-learning strategy. The novelty lies in expanding single-property d_{33} prediction to the simultaneous interpretation of d_{33}, T_d, and ε_r, while incorporating phase class, MPB characteristics, lattice distortion, stability-related factors, and configurational entropy as informative structural descriptors for describing composition/processing–property relationships. This framework provides a physically interpretable way to incorporate structural information into property prediction and to support the analysis of composition/processing–structure–property relationships.

2 Feature Selection and Data Preprocessing

2.1 Feature Selection

NBT-based ceramics are representative lead-free piezoelectric materials with an ABO_3-type perovskite structure. Their macroscopic electrical and electromechanical properties are synergistically governed by multiple structural factors, including A-site chemical disorder, B-site cation off-centering, [BO_6] oxygen-octahedral distortion, and phase-structure evolution. As illustrated in Fig. 1a, A-site cations such as Bi^{3+}/Na^+, B-site Ti^{4+} and its substituent ions, together with O^{2-} anions, constitute the fundamental perovskite crystal framework of NBT-based systems. A-site substitution mainly modulates lattice stability by tuning ionic-radius mismatch, the tolerance factor, and the degree of configurational disorder. In contrast, B-site substitution directly affects oxygen-octahedral distortion, local polarization instability, and the off-centering behavior of B-site cations.

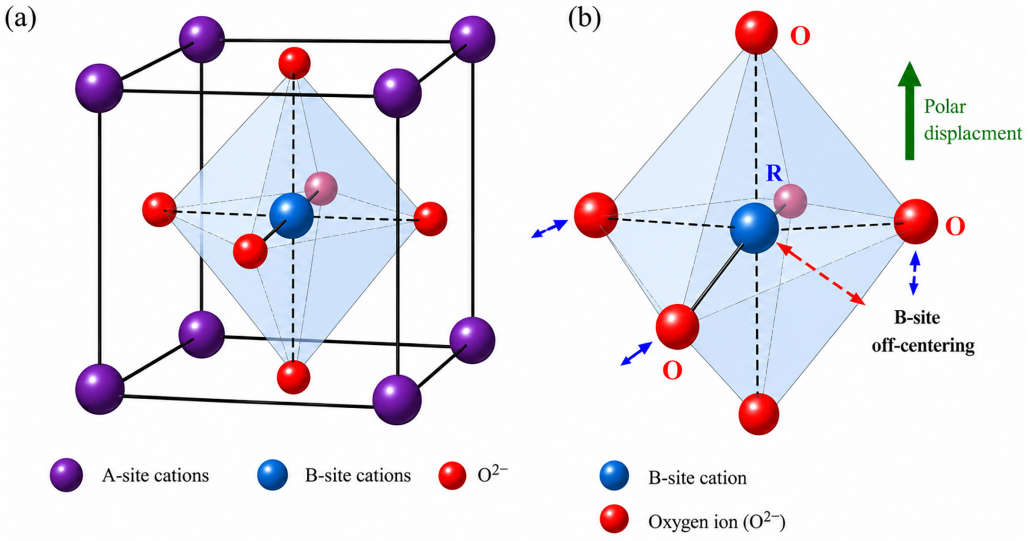

Figure 1: Schematic illustration of the NBT-based perovskite structure. (**a**) ABO3-type perovskite framework and (**b**) [BO_6] oxygen octahedron with B-site off-centering and octahedral distortion.

As shown in Fig. 1b, the displacement of B-site cations from the center of the oxygen octahedron, the tilting and elongation of oxygen octahedra, and the switching of local dipoles are key structural origins of the piezoelectric response in NBT-based ceramics. Therefore, based on the structural characteristics of NBT-based perovskites, constructing multi-source physics-informed descriptors that integrate chemical composition, processing parameters, structural features, and poling conditions provides a critical foundation for property prediction, mechanism interpretation, and composition design.

A total of 214 experimental records were collected from 34 publications. Among them, 204 records from 33 publications were used for model development, while 10 records from one additional publication were reserved for independent literature validation. The data acquisition mainly covered composition, processing parameters, phase-structure information, poling conditions, and electrical properties. Numerical values were preferentially extracted from tables in the original publications. When values were available only from figures, data were digitized and cross-checked according to the axis scales and original figure annotations to minimize extraction errors. Repeated records with identical composition, processing conditions, and property values were removed, while records with the same nominal composition but different sintering, calcination, phase state, or poling conditions were retained as independent experimental entries.

To improve reproducibility, all records were standardized in terms of composition representation, processing units, structural labels, poling conditions, and property units. The piezoelectric coefficient d_{33}, depolarization temperature T_d, and relative dielectric permittivity ε_r were selected as the target properties. Because not every publication reported all three target properties simultaneously, target-specific valid datasets were constructed. A sample was regarded as valid for a given target only when the target value and the required input descriptors were available after preprocessing. After target-specific filtering of the model-development dataset, 142, 133, and 121 valid samples were retained for d_{33}, T_d, ε_r, respectively, as summarized in Table 1. The full data acquisition strategy, reference sources, descriptor definitions, and target-specific filtering procedure are provided in Appendix A.

Table 1: Summary of target-specific datasets used for property prediction.

Target	Valid Samples	Unit	Main Source of Uncertainty
d_{33}	142	pC/N	Poling parameters, MPB flag, phase class, distortion score
T_d	133	°C	Phase class, MPB flag, tolerance factor, lattice distortion, thermal processing
ε_r	121	—	Calcination/sintering parameters, phase class, structural disorder, poling parameters

After data cleaning, unit standardization, missing-value processing, and outlier inspection, the statistical distributions of the three target properties are presented in Fig. 2. The constructed database incorporates information on A-site and B-site elemental compositions, ionic-radius-related parameters, lattice-stability factors, configurational entropy, calcination and sintering parameters, morphotropic phase boundary indicators, structural distortion degree, phase-structure categories, and poling conditions. These descriptors provide a physically meaningful representation of the complex nonlinear mapping relationships among compositional design, processing regulation, structural evolution, and functional properties in NBT-based ceramics.

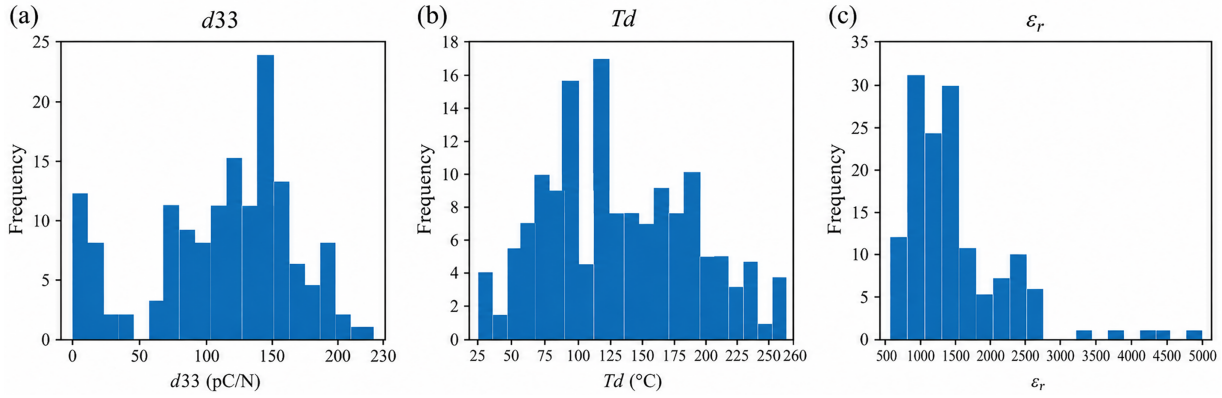

Figure 2: Statistical distributions of the target properties in the curated NBT-based lead-free piezoelectric ceramic dataset: (**a**) d_{33}, (**b**) T_d, and (**c**) ε_r.

On this basis, Extra Trees regression, DNNs, and ResNet-MLPs were employed to establish predictive models for d_{33}, T_d, and ε_r, respectively. Random five-fold cross-validation was used to evaluate the internal

predictive performance of the models. Furthermore, BNNs were introduced for probabilistic prediction and uncertainty quantification, providing reliability-related information for model outputs. In parallel, SHAP-based interpretability analysis was performed to identify the key descriptors influencing the target properties and to analyze the contribution patterns of composition, processing, structure, and poling conditions to property evolution.

Overall, this study aims to establish a data-driven research framework that integrates literature data mining, physics-informed descriptor construction, machine learning prediction, uncertainty assessment, and interpretability analysis. The proposed framework provides useful insights and methodological guidance for property optimization, mechanism understanding, and composition design of NBT-based lead-free piezoelectric ceramics.

The broad and nonuniform distributions of the three target properties indicate the heterogeneous nature of literature-derived ceramic datasets and highlight the necessity of cross-validation, uncertainty quantification, and interpretable analysis.

2.2 Methodology

As shown in Fig. 3, this study develops a two-stage structure-informed machine learning framework for NBT-based lead-free piezoceramics. Based on the 204-record model-development dataset, 35 candidate input descriptors were constructed from composition, processing, structural, and poling information to describe A-/B-site substitution, lattice distortion, phase evolution, and domain-orientation effects.

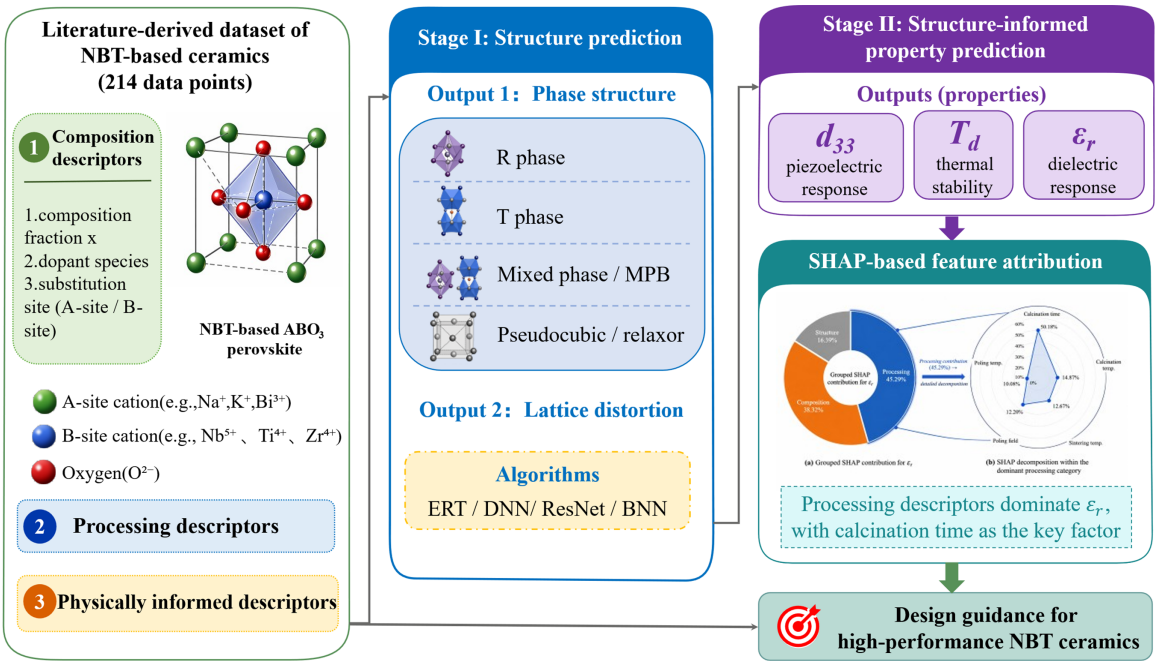

Figure 3: Schematic illustration of the proposed structure-informed machine-learning workflow for NBT-based lead-free piezoelectric ceramics.

To reduce feature redundancy and multicollinearity, pairwise Pearson correlation coefficients were calculated among the candidate input descriptors. Descriptor pairs with an absolute Pearson correlation coefficient greater than 0.95, i.e., $|r| > 0.95$, were considered highly correlated. Three highly correlated groups were identified:

{Zr_B, rB_variance, rB_mean, octahedral_factor}, {rA_mean, tolerance_factor},

and

{Ti_B, B_site_entropy}.

From these groups, rB_mean, rA_mean, and B_site_entropy were retained as representative descriptors. Accordingly, Zr_B, rB_variance, octahedral_factor, tolerance_factor, and Ti_B were removed, leaving 30 nonredundant input descriptors for subsequent model training.

The framework consists of two component-level modules: Stage I predicts structure-related labels from composition, processing, and poling descriptors, whereas Stage II predicts functional properties using the structure-informed descriptor system. It should be clarified that Stage II uses curated/experimentally assigned structural labels rather than the structure-related labels predicted by Stage I. Therefore, Stage I and Stage II are evaluated as two component-level modules in this study, rather than as a fully cascaded end-to-end prediction pipeline. MPB_flag, distortion_score, and phase_class_model were selected as structure-related labels, representing phase-boundary characteristics, lattice distortion/local instability, and effective phase state, respectively. Detailed definitions and encoding rules for these structural labels are provided in the Abbreviations section. These labels provide physically meaningful structural information that can improve the interpretability of composition/processing–property relationships. Here, "structure-informed" indicates the use of structural descriptors as informative physical features rather than a formally verified statistical or causal mediation relationship.

Subsequently, the structure-informed descriptor system was used to predict d_{33}, T_d, and ε_r using ETR, DNN, and ResNet-style MLP models under random five-fold cross-validation. BNNs and SHAP analysis were further employed for uncertainty quantification and interpretability analysis. This framework supports interpretable property prediction, candidate screening, and optimization of NBT-based lead-free piezoceramics within a composition/processing–structure–property paradigm.

For clarity, Fig. 3 groups the detailed phase labels into four broad structural families, whereas the Stage-I classifier uses the complete phase-label set defined in the Abbreviations section.

2.2.1 Descriptor Preprocessing and SHAP-Based Interpretability Analysis

The general machine-learning procedures used in this work, including correlation-based descriptor filtering, cross-validation-based preprocessing, deterministic regression, Bayesian uncertainty quantification, and SHAP-based interpretation, follow the methodology described in our previous study on KNN-based lead-free piezoceramics [1]. Therefore, the present section does not repeat the general algorithmic details, but instead focuses on the NBT-specific extension of this framework. The key methodological extension is the use of MPB_flag, distortion_score, and phase_class_model as informative structural descriptors linking composition/processing variables with the target properties d_{33}, T_d, and ε_r.

2.2.2 Model Construction and Comparative Learning Strategy

In contrast to our previous work, which mainly compared different neural-network architectures for KNN-based piezoceramics [1], the present study emphasizes the comparison of different model families for structure-informed property prediction in NBT-based lead-free piezoceramics. Considering the limited sample size, heterogeneous literature sources, and strong nonlinear composition–processing–structure–property coupling, ETR, DNN, and ResNet-style MLP were selected as representative models with complementary learning capabilities.

ETR was first adopted as a robust ensemble tree-based baseline because of its noise tolerance, ability to handle nonlinear feature interactions, and suitability for small heterogeneous literature-derived datasets. In this study, DNN and ResNet-style MLP models were included as nonlinear comparative models rather than being assumed to be superior to simpler models. Their use was intended to examine whether neural-network architectures could capture higher-order composition–processing–structure–property relationships beyond the tree-based baseline. All models were trained and evaluated using the same target-specific datasets, preprocessing workflow, descriptor set, and random five-fold cross-validation protocol. The prediction tasks for d_{33}, T_d, and ε_r were conducted independently to avoid the unnecessary loss of valid samples caused by missing values in unrelated targets. This comparative strategy was used to assess the predictive utility of the structure-informed descriptor system across different models. Nevertheless, due to the limited sample sizes, potential overfitting cannot be fully excluded. Therefore, the models should be regarded as tools for trend prediction, mechanism interpretation, and candidate screening, rather than substitutes for experimental validation. The overall architectures of these models are illustrated in Fig. 4.

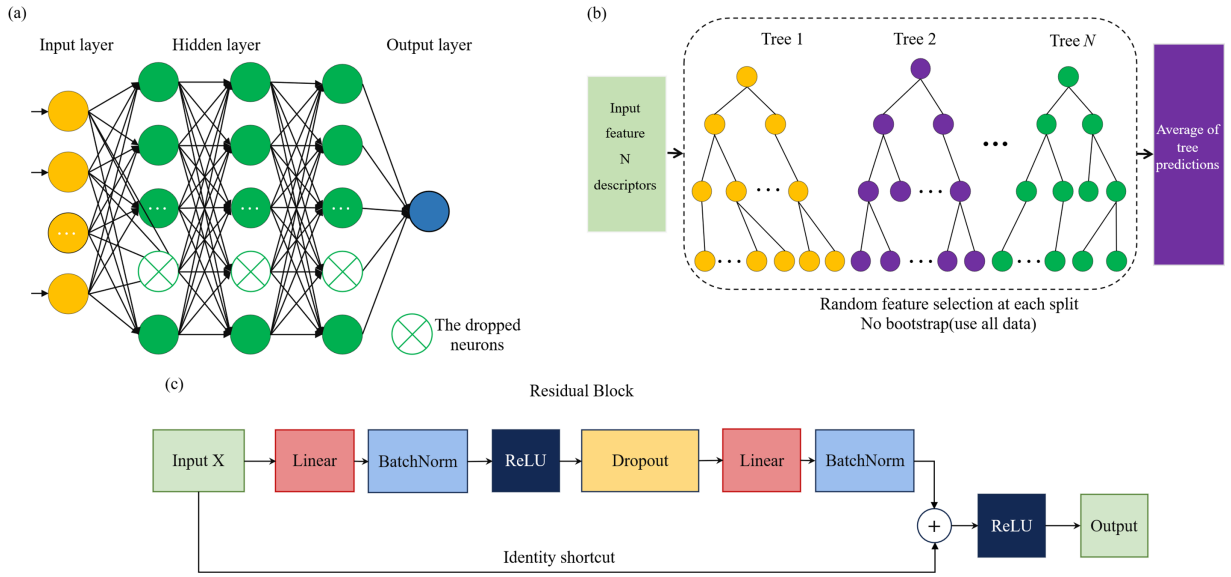

Figure 4: Schematic architectures of the three predictive models for NBT-based lead-free piezoceramics: (**a**) DNN, (**b**) ETR, and (**c**) ResNet-style MLP.

As shown in Fig. 4, ETR integrates multiple randomized decision trees, enabling effective handling of small sample sizes, high-dimensional descriptors, and nonlinear coupling relationships, while also providing feature-importance-based interpretability. The DNN relies on multilayer nonlinear transformations and exhibits strong capability for complex function approximation, making it suitable for capturing high-order correlations among composition, processing, structure, and poling conditions. Furthermore, ResNet introduces residual connections into the fully connected neural network architecture, which enhances information transmission and gradient propagation, thereby improving the stability of deep feature learning.

These three models represent ensemble tree-based learning, conventional deep neural networks, and residual deep neural networks, respectively. Their comparative use enables a systematic evaluation of differences in prediction accuracy, nonlinear modeling capability, and interpretability. The corresponding results are summarized in Table 2.

Table 2: Comparison of model architectures used in this study.

Model	Strategy	Strength	Limitation
ETR	Number of trees, maximum features, minimum samples per leaf, random seed	Robust ensemble baseline for small heterogeneous datasets	Limited rule transparency
DNN	Hidden layers, activation function, dropout, optimizer, learning rate	Nonlinear descriptor–property mapping	Sensitive to data scale
ResNet-style MLP	Residual blocks, hidden dimension, activation, dropout, optimizer	Stable deep feature learning	Weak feature interpretability
BNN	Prior distribution, variational inference, KL regularization, Monte Carlo sampling	Probabilistic prediction and uncertainty quantification	

Bayesian neural networks were used following the uncertainty-aware modeling strategy reported in Ref. [1]. In this work, the purpose of BNN modeling was not to re-establish the probabilistic learning theory, but to evaluate the reliability of predictions for NBT-based ceramics with incomplete and heterogeneous literature data. Multiple stochastic forward passes were performed to estimate the predictive mean and uncertainty interval for d_{33}, T_d, and ε_r. The resulting uncertainty information was further used to identify low-confidence samples associated with sparse data regions, complex phase evolution, or insufficiently reported processing and poling conditions. The network architecture is shown in Fig. 5.

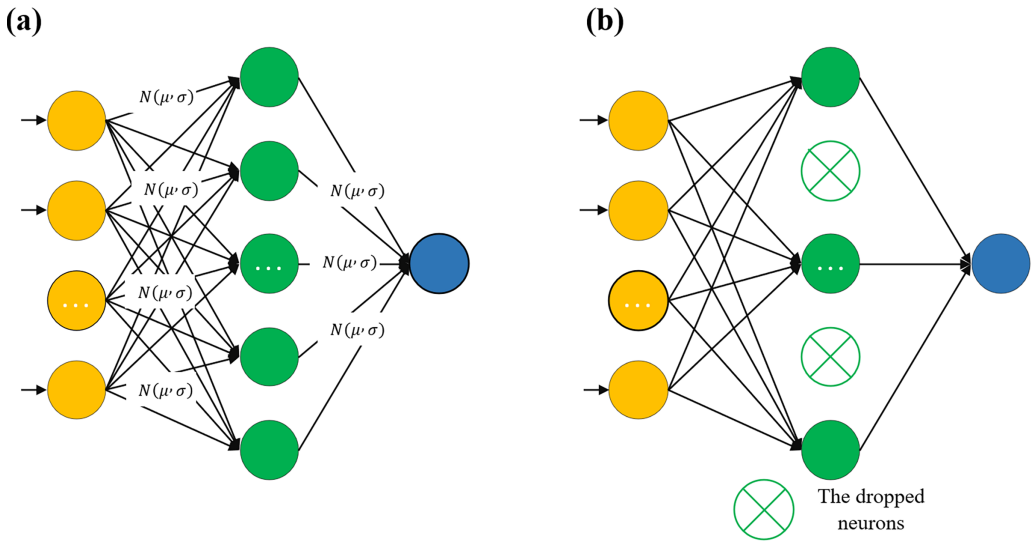

Figure 5: Schematic of two BNNs with (**a**) probabilistic weights and (**b**) probabilistic structure.

Detailed hyperparameter settings, model configurations, and key implementation details are summarized in Appendix B to ensure methodological transparency and reproducibility. The model performance

was evaluated using five-fold cross-validation and uncertainty analysis, and the results should be interpreted cautiously due to the limited size and heterogeneity of the literature-derived datasets.

For uncertainty quantification, the standard deviation obtained from BNN Monte Carlo sampling was regarded as model-related epistemic uncertainty. Considering that the dataset was collected from literature, additional experimental/data uncertainty may arise from differences in synthesis, processing, poling, measurement protocols, and data extraction. Since repeated-measurement standard deviations were generally unavailable, this uncertainty was estimated from validation residuals. The total predictive uncertainty was calculated as:

$$\sigma_{\text{total}}(x_i) = \sqrt{\sigma^2_{\text{model}}(x_i) + \sigma^2_{\text{data}}}$$

where σ_{model} is the epistemic uncertainty estimated by BNN Monte Carlo sampling, and σ_{data} is the validation-residual-estimated experimental/data uncertainty. The prediction intervals were then constructed as:

$$\hat{y}_i \pm k\sigma_{\text{total}}(x_i), k = 1, 2, 3$$

Prediction interval coverage probability (PICP) and expected calibration error (ECE) were further used to evaluate the calibration quality of the BNN uncertainty estimates. Calibration was evaluated at nominal coverage levels of 68.3%, 95.4%, and 99.7%, corresponding to the ±1σ, ±2σ, and ±3σ intervals, and ECE was calculated as the mean absolute difference between nominal and empirical coverage across these three levels. Coefficient of determination (R^2): Measures the proportion of variance explained by the model:

$$R^2 = 1 - \frac{\sum_{i=1}^{n}(y_i - \hat{y}_i)^2}{\sum_{i=1}^{n}(y_i - \bar{y})^2}$$

Root-mean-square error (RMSE): Quantifies absolute prediction errors.

$$\text{RMSE} = \sqrt{\frac{\sum_{i=1}^{n}(y_i - \hat{y}_i)^2}{n}}$$

Let y_i denote the experimentally measured output value for the i-th sample, $\hat{y}_i$ represent the corresponding model-predicted value, and $\bar{y}$ be the arithmetic mean of the observed dataset, where n is the total number of samples.

3 Results

3.1 Component-Level Evaluation of Structure-Related Label Prediction

Before final property prediction, Stage I was evaluated by predicting MPB_flag, distortion_score, and phase_class_model using composition, processing, and poling-related descriptors. The target structural label was excluded from the corresponding input set. After removing samples with missing values, 150 valid records were retained for this Stage-I evaluation. ETR-based classifiers were trained using random five-fold cross-validation to generate out-of-fold predictions for internal component-level evaluation.

As shown in Fig. 6, the out-of-fold predictions achieved accuracies of 0.873, 0.827, and 0.800 for MPB_flag, distortion_score, and phase_class_model, respectively, with a simultaneous prediction accuracy of 0.733. These results suggest that the selected descriptors contain useful information for estimating

structure-related labels in NBT-based ceramics. The best performance was obtained for MPB_flag, suggesting that morphotropic or relaxor phase-boundary characteristics are more readily reflected by the composition- and processing-related descriptors than the other two structure-related labels.

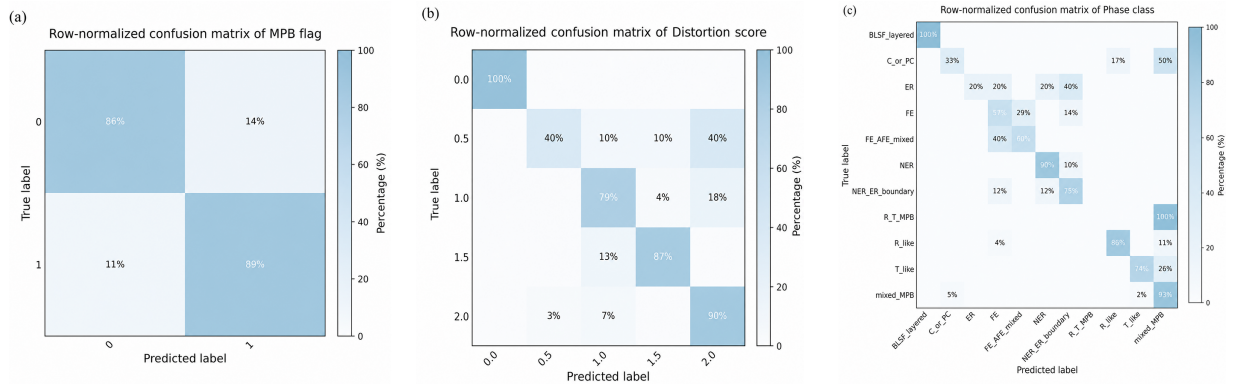

Figure 6: Row-normalized confusion matrices for the Stage-I component-level evaluation of structure-related label prediction in NBT-based lead-free piezoceramics. (**a**) MPB_flag (**b**) distortion_score (**c**) phase_class_model.

The distortion_score prediction shows moderate accuracy, reflecting its dependence on ionic-radius mismatch, tolerance-factor deviation, octahedral stability, configurational disorder, and thermal-processing history. By contrast, phase_class_model is more difficult to predict because of multiple phase categories and class imbalance. Here, ER and NER denote ergodic and nonergodic relaxor states, respectively; the complete phase abbreviations and fixed label encodings used in Fig. 6 are provided in the Abbreviations section. Thus, the Stage-I model is more suitable for identifying relatively dominant or well-represented structural categories than for distinguishing minority phase classes with limited training samples.

3.2 Component-Level Evaluation of Structure-Informed Property Prediction

To evaluate the Stage-II property-prediction module, ExtraTreesRegressor, DNN, and ResNet-style MLP were trained to predict d_{33}, T_d, and ε_r using the structure-informed descriptor system under random five-fold cross-validation. Identical data partitioning, preprocessing, feature encoding, and evaluation metrics were used for all models to ensure a fair comparison within this internal evaluation. The corresponding out-of-fold experimental-vs-predicted results are shown in Fig. 7, where Fig. 7(a1–a3), Fig. 7(b1–b3), and Fig. 7(c1–c3) correspond to ETR, DNN, and ResNet-style MLP, respectively.

The out-of-fold predictions show clear positive correlations with experimental values, indicating that the descriptors capture key composition–processing–structure–property relationships in NBT-based lead-free piezoceramics. The scattered deviations from the parity line mainly reflect the heterogeneity of literature-derived data, including variations in raw materials, processing conditions, microstructure, poling, and measurement protocols. Thus, the models are intended for trend prediction and mechanism interpretation rather than as deterministic replacements for experimental validation.

Table 3 summarizes the best-performing model for each target based on the out-of-fold R^2 and RMSE obtained from random five-fold cross-validation. The 10 records from one additional publication were excluded from model development and used exclusively for independent literature validation.

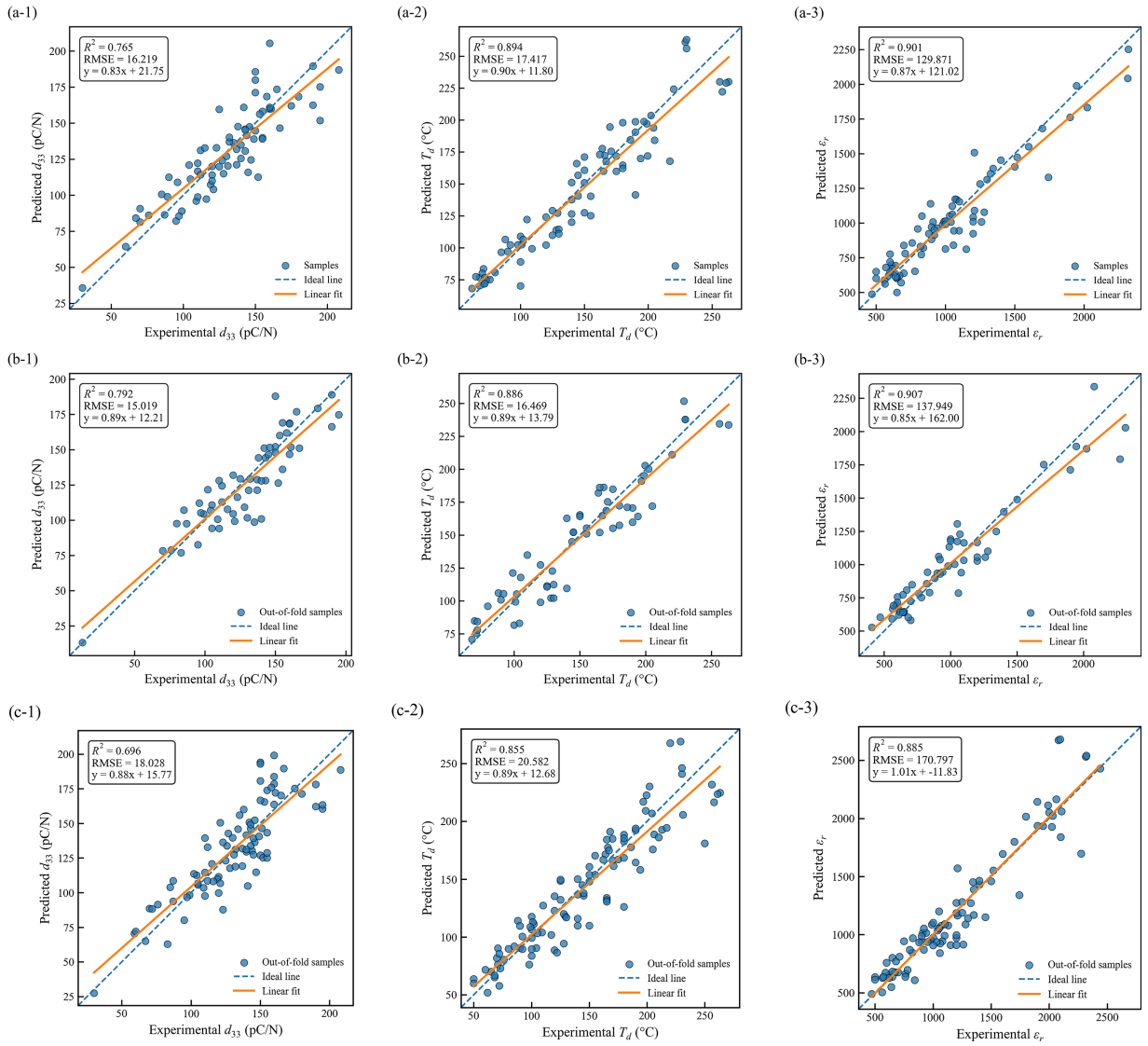

Figure 7: Experimental vs. predicted values of d_{33}, T_{d}, and ε_{r} obtained using five-fold cross-validation: (**a1**–**a3**) ETR, (**b1**–**b3**) DNN, and (**c1**–**c3**) ResNet-style MLP.

Table 3: Performance of the best-performing models under random five-fold cross-validation and independent literature validation.

Model	Target	R^2	RMSE	95% CI of R^2	95% CI of RMSE	Independent Literature-Validation RMSE
ETR	T_{d}	0.894	17.417	[0.754, 0.924]	[15.546, 30.805]	25.432
DNN	d_{33}	0.792	15.019	[0.702, 0.846]	[13.452, 19.003]	19.427
DNN	ε_{r}	0.907	137.949	[0.809, 0.934]	[122.486, 177.916]	188.148

The prediction performance varies among the three target properties, which may be related to their different physical origins and data completeness. T_d shows relatively stable prediction because it is strongly associated with phase stability, MPB characteristics, lattice distortion, tolerance factor, and thermal-processing history. In contrast, d_{33} is more difficult to predict due to its dependence on polarization rotation, domain-wall motion, phase-boundary instability, and poling-induced domain alignment. The prediction of ε_r is also challenging because it is sensitive to microstructure, defect chemistry, space-charge polarization, relative density, and measurement conditions that are often incompletely reported in literature-derived datasets.

From the model perspective, ETR provides a robust baseline for small heterogeneous datasets, DNN captures high-order nonlinear descriptor interactions, and ResNet-style MLP improves deep feature learning through residual connections. The target-dependent optimal models indicate that no single architecture is universally superior; instead, model suitability depends on the physical complexity and data characteristics of each property.

3.3 Uncertainty Analysis Using Bayesian Models

Deterministic models provide only point predictions and therefore cannot evaluate prediction confidence, which is a critical limitation for literature-derived ceramic datasets. In NBT-based lead-free piezoceramics, experimental uncertainty may arise from differences in composition design, calcination and sintering conditions, phase heterogeneity, poling procedures, and measurement protocols. Therefore, Bayesian neural networks were employed to further assess the reliability of model predictions.

In the BNN model, network weights are treated as probability distributions rather than fixed parameters. Multiple stochastic forward passes were performed to obtain the predictive mean and standard deviation, and the prediction intervals were expressed as ±1σ, ±2σ, and ±3σ. In this work, the ±3σ interval was used as the main confidence boundary to identify low-confidence predictions and potential extrapolation regions.

As shown in Fig. 8, the BNN-predicted mean values generally follow the experimental trends for d_{33}, T_d, and ε_r, indicating that the Bayesian model captures the major composition–processing–structure–property relationships while providing uncertainty information. Among the three target properties, T_d exhibits relatively narrower uncertainty intervals, suggesting that depolarization behavior is mainly controlled by more stable structural factors, including phase stability, lattice distortion, MPB characteristics, and thermal-processing history. In contrast, d_{33} shows broader uncertainty because the piezoelectric response is strongly affected by polarization rotation, domain-wall motion, phase-boundary instability, and poling-induced domain alignment. The largest uncertainty is observed for ε_r, reflecting its high sensitivity to microstructure, defect chemistry, space-charge polarization, frequency dispersion, and measurement conditions that are often incompletely reported in literature-derived datasets.

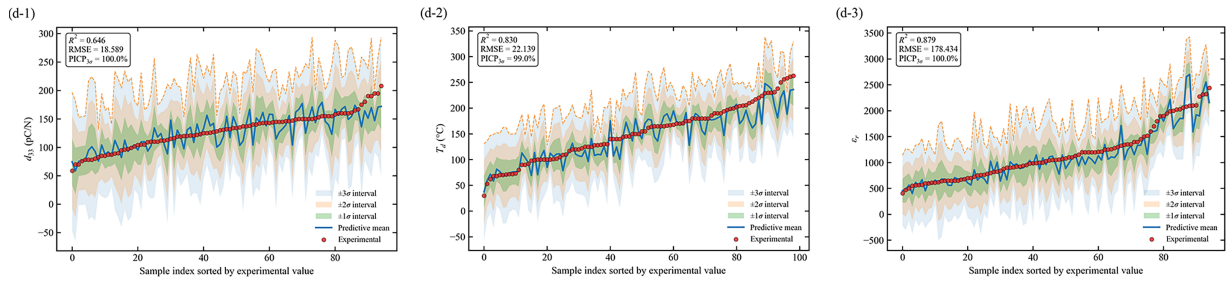

Figure 8: BNN-predicted uncertainty intervals for (**d-1**) d_{33}, (**d-2**) T_d, and (**d-3**) ε_r in NBT-based lead-free piezoceramics. The solid line represents the predictive mean, and the shaded regions denote the ±1σ, ±2σ, and ±3σ uncertainty intervals.

These results demonstrate that prediction uncertainty is closely related to the physical complexity and data completeness of each target property. Samples located near or outside the ±3σ boundary can be regarded as low-confidence predictions and should be treated with caution in subsequent experimental screening. Therefore, BNN-based uncertainty quantification provides not only predicted property values but also a reliability-aware criterion for evaluating candidate NBT-based lead-free piezoceramics.

Based on the calibration procedure described in Section 2.2.2, PICP and ECE were calculated to evaluate the reliability of the BNN uncertainty estimates. As shown in Table 4, the $PICP_{3\sigma}$ values are 100.0%, 99.0%, and 100.0% for d_{33}, T_d, and ε_r, respectively, indicating that the 3σ prediction intervals provide conservative coverage of the experimental observations. The ECE values are 6.1%, 3.2%, and 4.5%, respectively, suggesting acceptable calibration performance.

Table 4: Predictive performance and uncertainty calibration metrics of the Bayesian neural network model for d_{33}, T_d, and ε_r.

Target	R^2	RMSE	$PICP_{3\sigma}$	ECE
d_{33}	0.646	18.589	100.0%	6.1%
T_d	0.830	22.139	99.0%	3.2%
ε_r	0.879	178.434	100.0%	4.5%

3.4 SHAP-Based Interpretation of Dielectric Permittivity Prediction

To interpret the prediction of relative dielectric permittivity ε_r, SHAP analysis was performed using the mean absolute SHAP values of the input descriptors. Because the ε_r model exhibited relatively high predictive accuracy and stable fitting performance, it was selected as a representative case for the main-text interpretability analysis. The corresponding SHAP results for d_{33} and T_d are provided in Appendix B.3. The top-20 descriptors for ε_r were grouped into three physically meaningful categories: composition, processing, and structure, to clarify their relative contributions to the dielectric response.

As shown in Fig. 9a, processing-related descriptors contribute the most, accounting for 45.29% of the total SHAP weight, followed by composition-related descriptors with 38.32% and structure-related descriptors with 16.39%. This result indicates that ε_r in NBT-based lead-free piezoceramics is not determined solely by nominal composition, but is strongly affected by processing-induced structural evolution. Thermal processing and poling conditions can regulate phase formation, chemical homogeneity, defect concentration, grain growth, and domain configuration, thereby influencing dielectric polarization.

Fig. 9b further decomposes the processing contribution into individual variables. Calcination time shows the largest contribution, accounting for 50.18% of the processing-related SHAP weight, followed by calcination temperature, sintering temperature, poling field, and poling temperature, with contributions of 14.87%, 12.67%, 12.20%, and 10.08%, respectively. These variables are closely related to reaction completeness, phase purity, densification, defect redistribution, and domain alignment.

The dominant role of calcination-related parameters is physically reasonable. Insufficient calcination may lead to incomplete solid-state reaction, residual secondary phases, local compositional fluctuation, and nonuniform defect distribution, whereas excessive thermal treatment may promote A-site volatilization and modify defect chemistry. These effects can alter space-charge polarization, local lattice distortion, and dielectric relaxation behavior. Therefore, optimizing ε_r in NBT-based ceramics requires coordinated control of composition, calcination/sintering conditions, structural evolution, and poling parameters.

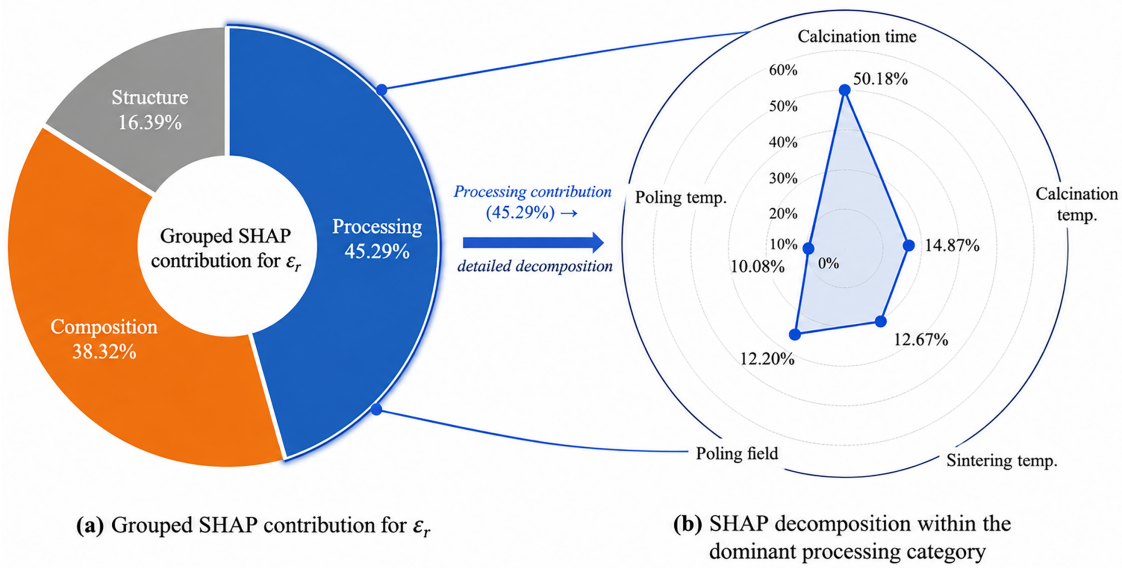

Figure 9: SHAP-based interpretation of ε_r prediction. (**a**) Grouped SHAP contributions of the top-20 descriptors. (**b**) Detailed decomposition of the dominant processing category.

Overall, the SHAP results provide a hierarchical interpretation of ε_r prediction and establish an interpretable link between machine-learning outputs and the processing–structure–property relationship in NBT-based lead-free piezoceramics.

4 Conclusion

In this work, a structure-informed machine learning framework was developed to predict and interpret the electrical properties of NBT-based lead-free piezoceramics. Model development used 204 records from 33 publications, while 10 records from one additional publication were reserved for independent literature validation. After Pearson correlation-based filtering using $|r| > 0.95$, 30 nonredundant descriptors were retained from 35 candidate descriptors. ETR, DNN, and ResNet-style MLP models were evaluated using random five-fold cross-validation, and the selected models were further assessed using the independent literature dataset. The results demonstrate that the proposed descriptor system effectively captures nonlinear composition–processing–structure–property relationships in NBT-based ceramics.

Bayesian neural network analysis further provides uncertainty-aware predictions and identifies low-confidence regions associated with data sparsity, experimental heterogeneity, and property-specific physical complexity. SHAP analysis reveals that processing parameters, composition-related descriptors, MPB characteristics, lattice-stability factors, and A-site configurational disorder dominate property variation. In particular, calcination-related parameters strongly influence dielectric permittivity, emphasizing the critical role of thermal processing in phase formation, defect regulation, and polarization response.

Overall, this study suggests that structural descriptors can provide useful intermediate physical information for improving the interpretability of composition/processing–property relationships in NBT-based lead-free piezoceramics. Formal mediation analysis and systematic descriptor ablation remain subjects for future investigation. The proposed framework provides a physically interpretable and reliability-aware strategy for data-driven design and optimization of high-performance NBT-based lead-free piezoceramics.

Acknowledgement: The authors sincerely appreciate the valuable suggestions provided by all the teachers during the manuscript revision process.

Funding Statement: This research was funded by the Postgraduate Education Reform and Quality Improvement Project of Henan Province, grant numbers YJS2023JD52 and YJS2025GZZ48; the Zhumadian 2023 Major Science and Technology Special Project, grant number ZMDSZDZX2023002; and the Scientific Research Foundation of Graduate School of Xinyang Normal University, grant number 2025KYJJ116.

Author Contributions: The authors confirm contribution to the paper as follows: conceptualization, algorithm design, and writing—original draft preparation, Yalong Liang; methodological suggestions and validation assistance, Xiaohui Yuan; data collection and curation, Yuning Han; writing—review and editing, project administration, and visualization, Pei Li. All authors reviewed and approved the final version of the manuscript.

Availability of Data and Materials: The curated dataset used in this study is provided as the Supplementary Material file Data.xlsx. The file contains the data prior to model-specific preprocessing, including normalization, feature screening, and dataset splitting. The source code is not publicly available. To facilitate reproducibility, the preprocessing workflow, model architectures, hyperparameter-selection procedure, final model settings, and key implementation details are described in Sections 2.2.1 and 2.2.2 and Appendix B.

Ethics Approval: Not applicable. This study did not involve humans or animals.

Conflicts of Interest: Given his role as guest editor of this journal, Pei Li had no involvement in the peer review of this article and had no access to information regarding its peer review. Full responsibility for the editorial process for this article was delegated to another journal editor. The authors declare no conflicts of interest.

Supplementary Materials: The supplementary material is available online at https://www.techscience.com/doi/10.32604/cmc.2026.086403/s1.

Abbreviations

The following abbreviations, descriptors, and structural-label encoding rules are used in this manuscript:

NBT	Sodium bismuth titanate, $Bi_{0.5}Na_{0.5}TiO_3$
MPB	Morphotropic phase boundary
ER	Ergodic relaxor
NER	Nonergodic relaxor
FE	Ferroelectric
AFE	Antiferroelectric
PC	Pseudocubic
BLSF	Bismuth-layer-structured ferroelectric
ETR	ExtraTreesRegressor
MLP	Multilayer perceptron
SHAP	Shapley additive explanations
PICP	Prediction interval coverage probability
ECE	Expected calibration error
MPIW	Mean prediction interval width
NMPIW	Normalized mean prediction interval width
C	Cubic
R	Rhombohedral
T	Tetragonal
Bi_A	Molar fraction of Bi at A-site
Na_A	Molar fraction of Na at A-site
Ba_A	Molar fraction of Ba at A-site
K_A	Molar fraction of K at A-site
Li_A	Molar fraction of Li at A-site

Sr_A	Molar fraction of Sr at A-site
La_A	Molar fraction of La at A-site
Y_A	Molar fraction of Y at A-site
Pr_A	Molar fraction of Pr at A-site
Gd_A	Molar fraction of Gd at A-site
Ho_A	Molar fraction of Ho at A-site
Yb_A	Molar fraction of Yb at A-site
Sm_A_or_additive	Molar fraction of Sm or additive at A-site
Ti_B	Molar fraction of Ti at B-site
Zr_B	Molar fraction of Zr at B-site
Nb_B	Molar fraction of Nb at B-site
Sb_B_or_additive	Molar fraction of Sb or additive at B-site
rA_mean	Average ionic radius of A-site ions (Å)
rA_variance	Variance of A-site ionic radius ($Å^2$)
rB_mean	Average ionic radius of B-site ions (Å)
rB_variance	Variance of B-site ionic radius ($Å^2$)
tolerance_factor	Goldschmidt tolerance factor
octahedral_factor	Octahedral factor (B-O geometry match)
A_site_entropy	Configurational entropy of A-site
B_site_entropy	Configurational entropy of B-site
calcination_temp_C	Calcination temperature (°C)
calcination_time_h	Calcination time (h)
sintering_temp_C	Sintering temperature (°C)
sintering_time_h	Sintering time (h)
MPB_flag	Binary MPB indicator: 0 = non-MPB; 1 = MPB
distortion_score	Ordinal distortion level: 0, 0.5, 1.0, 1.5, or 2.0
phase_class_model	Phase classification (0 = BLSF_layered; 1 = C_or_PC; 2 = ER; 3 = FE; 4 = FE_AFE_mixed; 5 = NER; 6 = NER_ER_boundary; 7 = R_T_MPB; 8 = R_like; 9 = T_like; 10 = mixed_MPB)
poling_temp_C	Poling temperature (°C)
poling_time	Poling time (min or h)
poling_field_kVmm	Poling electric field (kV/mm)
d_{33}	Piezoelectric coefficient d_{33} (pC/N)
T_d	Depolarization temperature T_d (°C)
ε_r	Relative permittivity ε_r

Appendix A

The initial data collection referred to References [3–12,31–50] in this manuscript, which constituted the primary literature pool. During subsequent data cleaning, data from references [39,46] that did not satisfy the final inclusion criteria for NBT-based ceramics were excluded from the final dataset. In addition, other relevant publications were also consulted but are not individually listed here. The main descriptors collected in this study are presented in the Abbreviations section. After Pearson correlation-based redundancy filtering, 30 nonredundant input descriptors were retained from the initial 35 candidate input descriptors. The Pearson correlation heatmap of the 38 variables, including 35 candidate input descriptors and three target properties, is shown in Fig. A1.

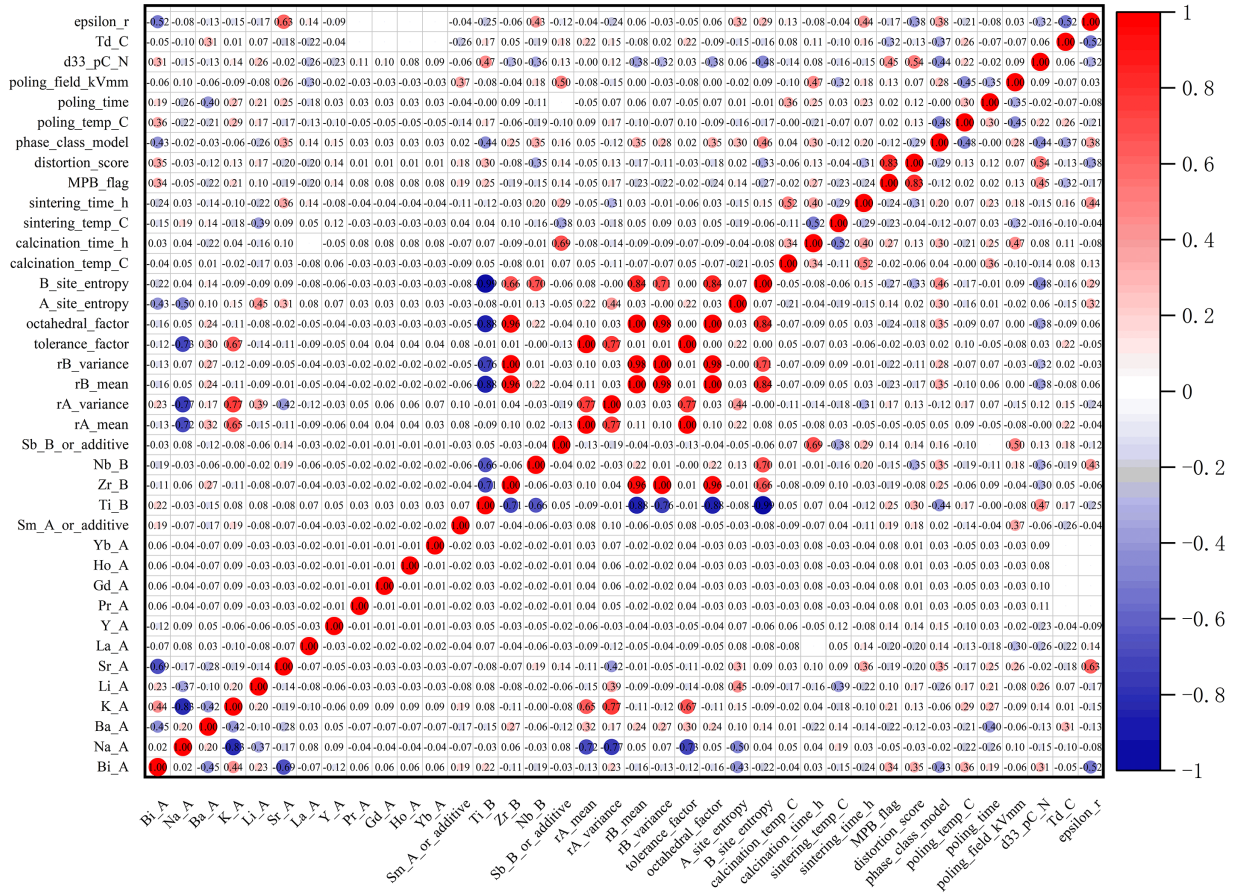

Figure A1: Pearson correlation heatmap of the 38 variables, including 35 candidate input descriptors and three target properties.

Appendix B

Appendix B.1

The final hyperparameter settings used in this study are summarized in Table A1. The input layer contained 30 neurons, corresponding to the 30 nonredundant descriptors retained after Pearson correlation-based filtering. The deterministic DNN and ResNet-style MLP models used MSELoss as the objective function, while the BNN used Gaussian negative log-likelihood loss with Kullback–Leibler divergence regularization for probabilistic learning. Hyperparameters were selected by grid search over predefined candidate ranges within the five-fold cross-validation framework. Bayesian optimization was not used in this study. To reduce training variability, the random seed was fixed at 42. For uncertainty estimation, 100 Monte Carlo stochastic forward passes were performed to calculate the predictive mean and uncertainty interval.

Table A1: Neural network hyperparameter settings.

Number of Neurons	**Input Layer** **Hidden Layer** **Output Layer**	**30** **128 × 256 × 128** **1**
Activation Function	SiLU (Swish); Tanh; Relu; SELU	
Dropout Rate	0.1–0.2	
Number of Epochs	4000–20,000	
Loss Function	Gaussian NLL Loss; MSELoss; Kullback–Leibler Divergence; MAELoss; Smooth L1 Loss	
Optimizer	AdamW; SGD; Adam; SparseAdam	
MC Dropout	50–250	

Appendix B.2

Key Code(ResNet-style MLP)

```
class ResidualBlock(nn.Module):
    def __init__(self, input_dim, output_dim, dropout_rate = 0.2):
        super(ResidualBlock, self).__init__()
        self.linear1 = nn.Linear(input_dim, output_dim)
        self.bn1 = nn.BatchNorm1d(output_dim)
        self.relu = nn.ReLU()
        self.dropout = nn.Dropout(dropout_rate)
        self.linear2 = nn.Linear(output_dim, output_dim)
        self.bn2 = nn.BatchNorm1d(output_dim)
        if input_dim != output_dim:
            self.shortcut = nn.Sequential(
                nn.Linear(input_dim, output_dim),
                nn.BatchNorm1d(output_dim)
            )
        else:
            self.shortcut = nn.Identity()
    def forward(self, x):
        identity = self.shortcut(x)
        out = self.linear1(x)
        out = self.bn1(out)
        out = self.relu(out)
        out = self.dropout(out)
        out = self.linear2(out)
        out = self.bn2(out)
        out += identity
        out = self.relu(out)
return out
```

Appendix B.3

Fig. A2 presents the SHAP contribution analysis of the optimal model for d_{33} prediction. The results show that structure-related descriptors dominate the prediction, accounting for 65.94% of the total

contribution. Among them, the mixed MPB phase, distortion score, ER phase, MPB flag, and NER phase are identified as the key contributing factors.

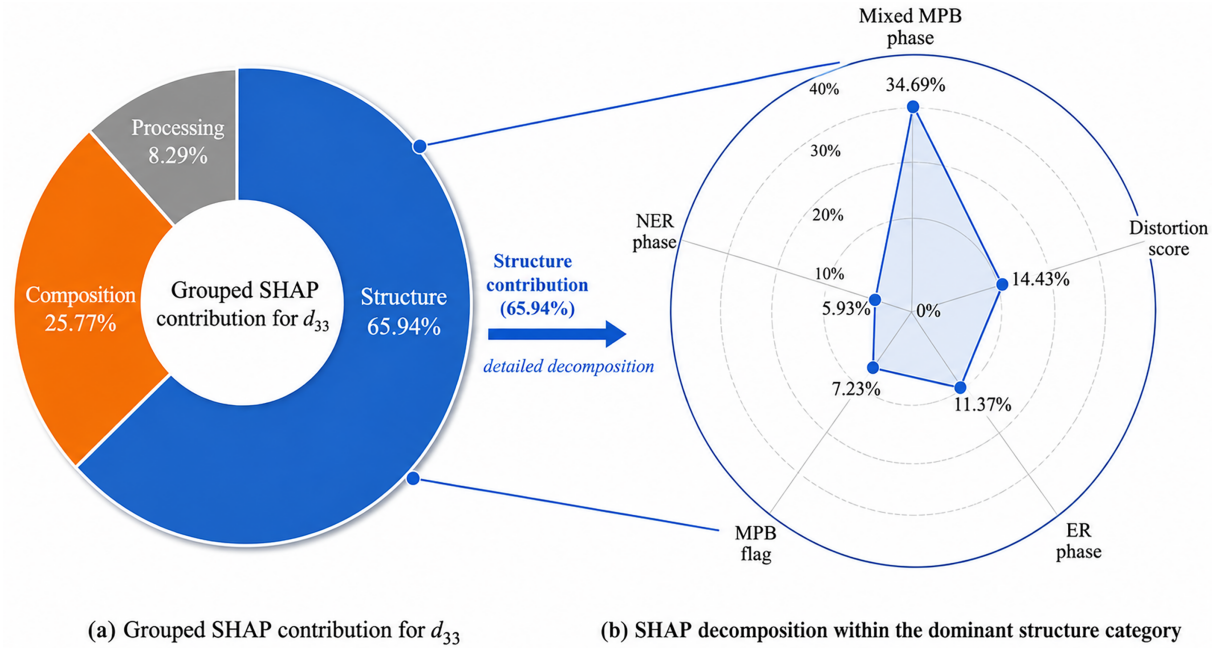

(a) Grouped SHAP contribution for d_{33} (b) SHAP decomposition within the dominant structure category

Figure A2: Grouped SHAP contribution and dominant structural-feature decomposition for d33 prediction.

Fig. A3 presents the SHAP contribution analysis of the optimal model for T_d prediction. Composition descriptors exhibit the largest contribution, accounting for 42.15% of the total SHAP weight. The dominant contributors are mainly Na_A, Sm_A or additive, K_A, Bi_A, and Ba_A, indicating that A-site compositional regulation plays an important role in governing the depolarization behavior.

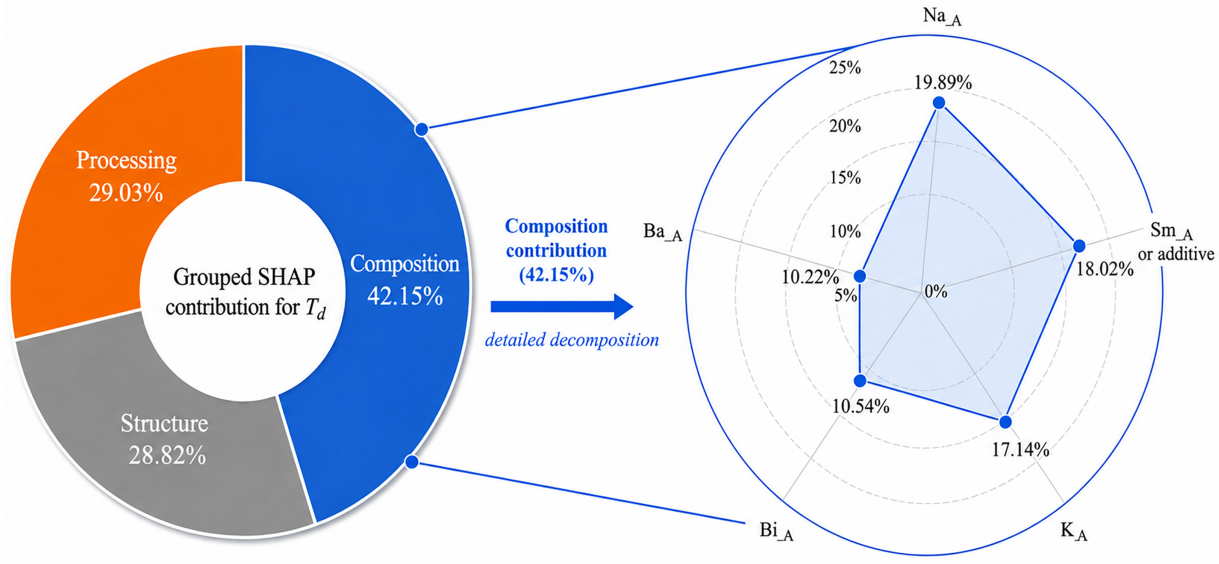

(a) Grouped SHAP contribution for T_d (b) SHAP decomposition within the dominant composition category

Figure A3: Grouped SHAP contribution and dominant compositional-feature decomposition for Td prediction.

References

1. Yuan X, Liang Y, Lu B, Zhao G, Li P. Interpretable machine learning with prediction uncertainty quantification for d33 in $(K_{0.5}Na_{0.5})$ NbO_3-based lead-free piezoelectric ceramics. Materials. 2026;19(5):948. doi:10.3390/ma19050948.
2. Wang S, Liang Y, Huang L, Li P. Cuckoo search-deep neural network hybrid model for uncertainty quantification and optimization of dielectric energy storage in $Na_1/\mathbf{2}Bi_{1/2}TiO_3$-based ceramic capacitors. Comput Mater Contin. 2025;85(2):2729–48. doi:10.32604/cmc.2025.068351.
3. Zhang X, Liang Y, Wang J, Chen P, Li P. Prediction of piezoelectric properties of NBT-based ceramics based on deep neural networks. Sci Prog. 2025;108(3):1–26. doi:10.1177/00368504251359081.
4. Xu C, Lin D, Kwok KW. Structure, electrical properties and depolarization temperature of $(Bi_{0.5}Na_{0.5})TiO_3$–$BaTiO_3$ lead-free piezoelectric ceramics. Solid State Sci. 2008;10(7):934–40. doi:10.1016/j.solidstatesciences.2007.11.003.
5. Chu BJ, Chen DR, Li GR, Yin QR. Electrical properties of $Na_1/2Bi_1/2TiO_3$–$BaTiO_3$ ceramics. J Eur Ceram Soc. 2002;22(13):2115–21. doi:10.1016/S0955-2219(02)00027-4.
6. Swain S, Kumar Kar S, Kumar P. Dielectric, optical, piezoelectric and ferroelectric studies of NBT–BT ceramics near MPB. Ceram Int. 2015;41(9):10710–7. doi:10.1016/j.ceramint.2015.05.005.
7. Lin D, Kwok KW, Chan HLW. Structure and electrical properties of $Bi_{0.5}Na_{0.5}TiO_3$–$BaTiO_3$–$Bi_{0.5}Li_{0.5}TiO_3$ lead-free piezoelectric ceramics. Solid State Ion. 2008;178(37–38):1930–7. doi:10.1016/j.ssi.2007.12.096.
8. Kanuru SR, Baskar K, Dhanasekaran R. Synthesis, structural, morphological and electrical properties of NBT–BT ceramics for piezoelectric applications. Ceram Int. 2016;42(5):6054–64. doi:10.1016/j.ceramint.2015.12.162.
9. Liu G, Dong J, Zhang L, Yan Y, Jing R, Jin L. Phase evolution in $(1–x)(Na_{0.5}Bi_{0.5})TiO_3$-$xSrTiO_3$ solid solutions: a study focusing on dielectric and ferroelectric characteristics. J Mater. 2020;6(4):677–91. doi:10.1016/j.jmat.2020.05.005.
10. Lin D, Zheng Q, Xu C, Kwok KW. Structure, electrical properties and temperature characteristics of $Bi_{0.5}Na_{0.5}TiO_3$–$Bi_{0.5}K_{0.5}TiO_3$–$Bi_{0.5}Li_{0.5}TiO_3$ lead-free piezoelectric ceramics. Appl Phys A. 2008;93(2):549–58. doi:10.1007/s00339-008-4667-z.
11. Kantha P, Pisitpipathsin N. Effect of $KNbO_3$ addition on diffuse phase transition and dielectric properties of $Bi_{0.5}Na_{0.5}TiO_3$ ceramics. Integr Ferroelectr. 2018;187(1):129–37. doi:10.1080/10584587.2018.1444884.
12. Chen P, Yuan B, Wang J, Zhang X, Chen Y, Cao F, et al. Enhanced piezoelectric response of $Na_{0.5}Bi_{0.5}TiO_3$–$BaTiO_3$ lead free ceramics by tuning the local polar heterogeneity. Mater Res Bull. 2025;184(4):113231. doi:10.1016/j.materresbull.2024.113231.
13. Ramprasad R, Batra R, Pilania G, Mannodi-Kanakkithodi A, Kim C. Machine learning in materials informatics: recent applications and prospects. npj Comput Mater. 2017;3(1):54. doi:10.1038/s41524-017-0056-5.
14. Li L, Xu K, Su R, Gu H, Ma P. AI as a catalyst for transforming scientific research: a perspective. AI Agent. 2025;1(1):8. doi:10.20517/aiagent.2025.08.
15. Xie T, Grossman JC. Crystal graph convolutional neural networks for an accurate and interpretable prediction of material properties. Phys Rev Lett. 2018;120(14):145301. doi:10.1103/PhysRevLett.120.145301.
16. Tao Q, Xu P, Li M, Lu W. Machine learning for perovskite materials design and discovery. npj Comput Mater. 2021;7(1):23. doi:10.1038/s41524-021-00495-8.
17. Balachandran PV, Kowalski B, Sehirlioglu A, Lookman T. Experimental search for high-temperature ferroelectric perovskites guided by two-step machine learning. Nat Commun. 2018;9(1):1668. doi:10.1038/s41467-018-03821-9.
18. Ma B, Wu X, Zhao C, Lin C, Gao M, Sa B, et al. An interpretable machine learning strategy for pursuing high piezoelectric coefficients in $(K_{0.5}Na_{0.5})NbO_3$-based ceramics. npj Comput Mater. 2023;9(1):229. doi:10.1038/s41524-023-01187-1.
19. Ouyang R, Curtarolo S, Ahmetcik E, Scheffler M, Ghiringhelli LM. SISSO: a compressed-sensing method for identifying the best low-dimensional descriptor in an immensity of offered candidates. Phys Rev Mater. 2018;2(8):083802. doi:10.1103/physrevmaterials.2.083802.
20. Li Q, Fu N, Omee SS, Hu J. MD-HIT: machine learning for material property prediction with dataset redundancy control. npj Comput Mater. 2024;10(1):245. doi:10.1038/s41524-024-01426-z.

21. Zhang D, Jia X, Wang Y, Liu H, Wang Q, Jang SH, et al. Digital materials ecosystem: from databases to AI agents for autonomous discovery. Chem Sci. 2026;17(12):5782–804. doi:10.1039/d5sc09229a.
22. Choudhary K, DeCost B, Chen C, Jain A, Tavazza F, Cohn R, et al. Recent advances and applications of deep learning methods in materials science. npj Comput Mater. 2022;8(1):59. doi:10.1038/s41524-022-00734-6.
23. Merchant A, Batzner S, Schoenholz SS, Aykol M, Cheon G, Cubuk ED. Scaling deep learning for materials discovery. Nature. 2023;624(7990):80–5. doi:10.1038/s41586-023-06735-9.
24. He K, Zhang X, Ren S, Sun J. Deep residual learning for image recognition. In: 2016 IEEE Conference on Computer Vision and Pattern Recognition (CVPR); 2016 Jun 27–30; Las Vegas, NV, USA. p. 770–8. doi:10.1109/cvpr.2016.90.
25. Batra R, Song L, Ramprasad R. Emerging materials intelligence ecosystems propelled by machine learning. Nat Rev Mater. 2021;6(8):655–78. doi:10.1038/s41578-020-00255-y.
26. Li L, Chang J, Vakanski A, Wang Y, Yao T, Xian M. Uncertainty quantification in multivariable regression for material property prediction with Bayesian neural networks. Sci Rep. 2024;14(1):10543. doi:10.1038/s41598-024-61189-x.
27. Abdar M, Pourpanah F, Hussain S, Rezazadegan D, Liu L, Ghavamzadeh M, et al. A review of uncertainty quantification in deep learning: techniques, applications and challenges. Inf Fusion. 2021;76(1):243–97. doi:10.1016/j.inffus.2021.05.008.
28. Lundberg SM, Erion G, Chen H, DeGrave A, Prutkin JM, Nair B, et al. From local explanations to global understanding with explainable AI for trees. Nat Mach Intell. 2020;2(1):56–67. doi:10.1038/s42256-019-0138-9.
29. Zhong X, Gallagher B, Liu S, Kailkhura B, Hiszpanski A, Han TY. Explainable machine learning in materials science. npj Comput Mater. 2022;8(1):204. doi:10.1038/s41524-022-00884-7.
30. Geurts P, Ernst D, Wehenkel L. Extremely randomized trees. Mach Learn. 2006;63(1):3–42. doi:10.1007/s10994-006-6226-1.
31. Parija B, Badapanda T, Rout SK, Cavalcante LS, Panigrahi S, Longo E, et al. Morphotropic phase boundary and electrical properties of $1–x[Bi_{0.5}Na_{0.5}]TiO_3–xBa[Zr_{0.25}Ti_{0.75}]O_3$ lead-free piezoelectric ceramics. Ceram Int. 2013;39(5):4877–86. doi:10.1016/j.ceramint.2012.11.080.
32. Rahman JU, Hussain A, Maqbool A, Ryu GH, Song TK, Kim WJ, et al. Field induced strain response of lead-free $BaZrO_3$-modified $Bi_{0.5}Na_{0.5}TiO_3–BaTiO_3$ ceramics. J Alloys Compd. 2014;593:97–102. doi:10.1016/j.jallcom.2014.01.031.
33. Moosavi A, Bahrevar MA, Aghaei AR, Ramos P, Algueró M, Amorín H. High-field electromechanical response of $Bi_{0.5}Na_{0.5}TiO_3–Bi_{0.5}K_{0.5}TiO_3$ across its morphotropic phase boundary. J Phys D Appl Phys. 2014;47(5):055304. doi:10.1088/0022-3727/47/5/055304.
34. Mesrar M, Elbasset A, Echatoui NS, Abdi F, Lamcharfi T. Microstructural and high-temperature dielectric, piezoelectric and complex impedance spectroscopic properties of $K_{0.5}Bi_{0.5}TiO_3$ modified NBT-BT lead-free ferroelectric ceramics. Heliyon. 2023;9(4):e14761. doi:10.1016/j.heliyon.2023.e14761.
35. Yang Z, Liu B, Wei L, Hou Y. Structure and electrical properties of $(1–x)Bi_{0.5}Na_{0.5}TiO_3–xBi_{0.5}K_{0.5}TiO_3$ ceramics near morphotropic phase boundary. Mater Res Bull. 2008;43(1):81–9. doi:10.1016/j.materresbull.2007.02.016.
36. Zhang Y, Chu R, Xu Z, Hao J, Chen Q, Peng F, et al. Piezoelectric and dielectric properties of Sm_2O_3-doped $0.82Bi_{0.5}Na_{0.5}TiO_3–0.18Bi_{0.5}K_{0.5}TiO_3$ ceramics. J Alloys Compd. 2010;502(2):341–5. doi:10.1016/j.jallcom.2010.03.241.
37. Aamir M, Ali Khan S, Ahmed T, Hussain A, Lee S. Effect of ferroelectric phase evolution on dielectric and piezoelectric properties in yttrium-doped BNT-BT ceramics. Solid State Sci. 2023;139:107169. doi:10.1016/j.solidstatesciences.2023.107169.
38. Tian Y, Liu C, Li S, Ye B, Zhao Z, Ji X, et al. Enhanced ferroelectric relaxation and mechanical properties of Sb_2O_3-modified BNT-based lead-free piezoelectric ceramics. Ceram Int. 2025;51(23):38381–9. doi:10.1016/j.ceramint.2025.06.071.
39. Satha S, Ben Achour MA, Rguiti M, Lorgouilloux Y, Courtois C. Comprehensive study of Al-doped $BaTiO_3$ ceramics: from doping optimization to electromechanical enhancement for piezoelectric applications. J Eur Ceram Soc. 2026;46(11):118330. doi:10.1016/j.jeurceramsoc.2026.118330.

40. Deng A, Wu J. Effects of rare-earth dopants on phase structure and electrical properties of lead-free bismuth sodium titanate-based ceramics. J Mater. 2020;6(2):286–92. doi:10.1016/j.jmat.2020.03.005.
41. Jarupoom P, Jaita P. Enhanced electrical and energy harvesting performances of lead-free BMT modified BNT piezoelectric ceramics. J Asian Ceram Soc. 2022;10(2):498–513. doi:10.1080/21870764.2022.2076362.
42. Ma Z, Nie W, Sun M, Li P, Liu L, Wang B, et al. Li^{+} and Nb^{5+} codoped BNT-based ceramic with ultrahigh electrostrain under a moderate electric field. J Adv Ceram. 2026;15(6):9221309. doi:10.26599/jac.2026.9221309.
43. Naeem F, Saleem M, Jabbar H, Tanvir G, Asif F, Baluch AH, et al. Enhanced ferroelectric and dielectric properties of niobium-doped lead-free piezoceramics. Materials. 2023;16(2):477. doi:10.3390/ma16020477.
44. He H, Lu X, Li M, Wang Y, Li Z, Lu Z, et al. Thermal and compositional driven relaxor ferroelectric behaviours of lead-free $Bi_{0.5}Na_{0.5}TiO_3$–$SrTiO_3$ ceramics. J Mater Chem C. 2020;8(7):2411–8. doi:10.1039/c9tc04864b.
45. Dong G, Wang L, Zhang Y, Yang N, Quan Y, Fei C, et al. Effect of Li^{+} doping on structural and electrical characteristics of BNBT-based ceramics. Ceram Int. 2025;51(26):51214–24. doi:10.1016/j.ceramint.2025.08.348.
46. Chen Y, Zhang CC, Qin L, Jiang CB, Liu KH, Ma C, et al. Enhanced dielectric and piezoelectric properties in $Na_{0.5}Bi_{4.5}Ti_4O_{15}$ ceramics with Pr-doping. Ceram Int. 2018;44(15):18264–70. doi:10.1016/j.ceramint.2018.07.037.
47. Prado A, Rubio-Marcos F, Ramajo L, Castro MS. Dielectric and ferroelectric properties evolution of $(1–x)(Bi_{0.5}Na_{0.5}TiO_3)–xK_{0.5}Na_{0.5}NbO_3$ piezoceramics. Bull Mater Sci. 2020;43(1):282. doi:10.1007/s12034-020-02246-9.
48. Wang Z, Zhao J, Niu G, Ren W, Zhang N, Zheng K, et al. Giant strain responses and relaxor characteristics in lead-free $(Bi_{0.5}Na_{0.5})TiO_3$–$BaZrO_3$ ferroelectric thin films. J Mater Chem C. 2022;10(19):7449–59. doi:10.1039/d1tc05197k.
49. Ullah A, Ishfaq M, Won Ahn C, Ullah A, Ehsan Awan S, Won Kim I. Relaxor behavior and piezoelectric properties of $Bi(Mg_{0.5}Ti_{0.5})O_3$-modified $Bi_{0.5}Na_{0.5}TiO_3$ lead-free ceramics. Ceram Int. 2015;41(9):10557–64. doi:10.1016/j.ceramint.2015.04.150.
50. Luo H, Qi H, Sun S, Wang L, Ren Y, Liu H, et al. Structural origin for the high piezoelectric performance of $(Na_{0.5}Bi_{0.5})TiO_3$-$BaTiO_3$-$BiAlO_3$ lead-free ceramics. Acta Mater. 2021;218:117202. doi:10.1016/j.actamat.2021.117202.